Superconductivity in the amorphous phase of the half-Heusler TiNiSn alloy

J. Barzola-Quiquia,[1,*] E. Osmic,[2] P. G. Bercoff,[3] L. Venosta,[3] and P. Häussler[1]

[1] *Division of Thin Films Physics, Institute of Physics, Chemnitz University of Technology, 09107 Chemnitz, Germany*

[2] *High Field Magnetic Laboratory Dresden (HLD-EMFL), Helmholtz Center Dresden-Rossendorf, D-01328 Dresden, Germany*

[3] *Universidad Nacional de Córdoba, Facultad de Matemática, Astronomía, Física y Computación (FAMAF). Instituto de Física Enrique Gaviola (IFEG), CONICET. Av. Medina Allende s/n, 5000 Córdoba, Argentina*

Amorphous TiNiSn films were prepared at $T \approx 4.2\,\mathrm{K}$ and resistance $R(T)$ and thermopower $S(T)$ have been investigated. $R(T)$ shows that the sample is superconducting and the transition temperature T_c increases with increasing annealing temperature, being the maximum $T_{c3} = 4.19\,\mathrm{K}$. The electron-phonon coupling estimated from $S(T)$ results is very close to the value calculated using McMillan equation for the superconducting transition T_c, indicating that amorphous TiNiSn is an intermediate electron-phonon coupled superconductor. After annealing up to $T = 850\,\mathrm{K}$, the amorphous sample crystallizes at $T_K \approx 785\,\mathrm{K}$. Atomic structure and high stability of the amorphous phase can be explained in the framework of electronically stabilized Hume-Rothery phases, where hybridization from Ti-d and Ni-d electrons plays an important role. The crystallized sample shows a well-ordered half-Heusler crystalline phase, space group $F\bar{4}3m$, with a TiNiSn atomic order in the unit cell instead of the common NiTiSn type.

I. INTRODUCTION

In recent years, Heusler [1] compounds have attracted the interest of the scientific community because of their enormous potential in diverse fields, ranging from spintronics [2], thermoelectric applications [3], to topological insulators [4]. Heusler alloys are intermetallic compounds, which can be divided into two categories, full-Heusler (FH) and half-Heusler (HH) alloys. The FH and HH alloys are ternary intermetallic alloys with the typical formula X_2YZ and XYZ respectively, where X and Y are usually transition metals and Z is a main group element. In addition to their well-know magnetic properties, superconducting properties have also been found in these materials. The first Heusler alloy superconductor was reported in 1982 by Ishikawa *et al.* [5] who studied the cubic FH alloys YPd_2Sn with a transition temperature of $T_c = 3.72\,\mathrm{K}$. This discovery has motivated experimentalists and theoreticians to investigate superconductivity in Heusler alloys, so to date there is a relatively good amount of compounds in the Heusler family known to be superconducting [6]. Superconductivity in HH alloys was also found, e.g. in YPtBi [7], ErPdBi [8], LuPtBi [9], etc. A very well-known HH alloy is TiNiSn, which is interesting because of its exceptional thermoelectrical properties [3]. TiNiSn and the above-mentioned HH alloys are systems with non-centrosymmetric crystallographic symmetry with space group $F\bar{4}3m$. The appearance of superconductivity in this crystal structure lacks a center of inversion, opening the possibility of unconventional Cooper pair states, i.e. a superconducting pairing state with a mixture of spin-singlet and spin-triplet components [10]. Experimental evidence of superconductivity in the crystalline phase of TiNiSn has not been reported as in the case of the other above-mentioned non-centrosymmetric HH alloys. Even when there are several studies on the electrical transport and magnetic properties of amorphous FH alloys reported in the literature, e.g. of $AlCu_2Mn$ [11] and Co_2MnGa[12,13], as far as we know, no studies of this kind have been published on amorphous HH alloys.

In the present work we have investigated the transport properties of amorphous TiNiSn after quenching from the gas phase at liquid ^{4}He temperature. By successively annealing and cooling we have studied the changes in the resistance $R(T)$ and thermopower $S(T)$. We have noticed an unexpected behavior in the $R(T)$, i.e. the observation of superconductivity at temperatures $T < 4.5\,\mathrm{K}$ when the alloy is still in amorphous phase, as determined by transmission electron diffraction. To this date, and to best of our knowledge, this is the first time the observation of superconductivity in the amorphous phase of a half-Heusler alloy is reported.

II. EXPERIMENTAL DETAILS

The initial TiNiSn alloy was prepared by argon arc melting stoichiometric proportions of the pure elements (Ti 99.99 %, Ni 99.994 %, Sn 99.998 %, by Alfa Aesar). After that, the millimeter-sized sample was milled into ~ 100 μm grains and introduced in a flash evaporation device [14]. This device consists of a chamber where the grains fall on an incandescent tungsten band going instantly from the solid phase to the gas phase. This vaporized material is quench-condensed on a substrate which is cooled at liquid ^{4}He temperature. With this technique we obtain a quenching rate in the order of $\approx 10^8 - 10^{10}$ K/min, which is much higher than the quenching rate achieved by melt-spinning[15]. This guarantees the formation of amorphous films without nanocrystalline grains or aggregates. Another advantage of

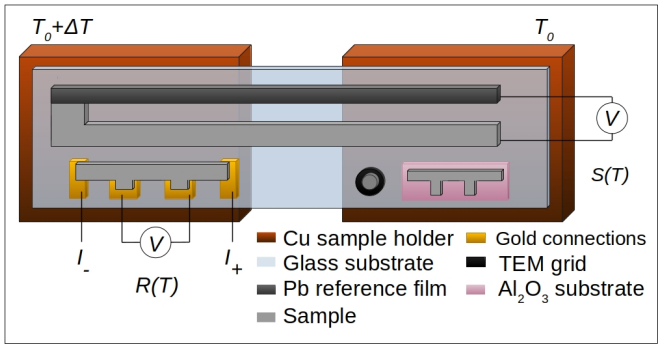

Fig. 1. Sketch of the *in-situ* prepared thin film for thermopower and resistance measurements. The TEM grid and the sample for T_K measurements (on Al_2O_3 substrate) are also shown.

this preparation method is the low uncertainty in the element concentration, which is in the order of $\lessapprox 0.1$ at.%[16,17] over an entire centimeter-sized sample. During deposition, the substrate is covered with a mask so that the samples used for the measurement of resistance $R(T)$, thermopower $S(T)$ and electron diffraction are obtained simultaneously. The experimental setup is schematized in Fig. 1. The complete thin film preparation process and measurements were performed *in-situ* at high vacuum conditions ($P \approx 10^{-8}$ mbar) inside a low temperature cryostat. Immediately after deposition, the resistance $R(T)$ and thermopower $S(T)$ were measured during annealing (irreversible changes) and after annealing (reversible changes). $S(T)$ was measured between 6 K and 345 K by applying a slowly alternating temperature gradient across the thin film. The advantage of this dynamical method is the suppression of spurious EMF's and offset drifts[18]. $R(T)$ was measured between 1.2 K and 345 K in a standard four-terminal geometry using a direct current of 5 µA. Structure investigations were performed *ex-situ* by electron diffraction (ED) in transmission, at room temperature in a commercial TEM, implemented with an energy filtered CCD camera. The data analyses for calculating the structure factor $SF(K)$ and the pair correlation function $g(r)$ were done with the standard methods described in Ref. [19]. To obtain the crystalline phase and estimate the crystallization temperature T_K of the amorphous TiNiSn film, we annealed the sample in a high temperature cryostat up to $T = 850$ K and afterwards, the ED experiment was repeated in order to determine the crystalline structure.

III. RESULTS AND DISCUSSION

A. Atomic structure

As mentioned before, the atomic structure was investigated *ex-situ* after the sample was annealed at $T_{ann3} = 345$ K. Additionally, in order to have information about the crystalline structure, a sample was annealed at $T_{ann4} = 850$ K. The raw data of the ED results are plotted in Fig. 2. From the diffraction results we can state that after annealing the sample at $T_{ann3} = 345$ K it is still in the amorphous state, while the one annealed at $T_{ann4} = 850$ K shows the presence of well-defined crystals. Using the standard method for analyzing diffraction results from amorphous materials[19] we have calculated the structure factor $SF(K)$ and the pair correlation function $g(r)$ for the amorphous phase; both results are plotted in Fig. 3. The obtained structure factor $SF(K)$ shows a dominant peak in K-space, followed by clear second and third peaks, indicating a long distance periodical order in the amorphous phase. By looking closely at the first peak in $SF(K)$, a shoulder at $K \approx 20\,\mathrm{nm}^{-1}$ can be observed, which —after annealing at 850 K— splits into the two first peaks of the crystalline phase, as it can be seen in Fig. 2. In r-space, the obtained pair correlation function $g(r)$ (Fig. 3b) shows a well-defined local and long range periodical order, i.e. very pronounced first nearest-neighbors correlation, up to the fourth nearest-neighbor. It was shown that amorphous materials formed from elements with s and p valence electrons which are stable above room temperature, are mostly semiconductors and insulators, such as a-(C, Ge, Si, Se, $Ge_{100-x}Sb_x$, $Ga_{100-x}Te_x$, etc.) and a-(SiO_2, AlO_2, etc.), respectively. Nevertheless, another big family of above-room-temperature stable amorphous materials based on alloys containing at least one transition metal (TM) with d and f valence electrons also exists, e.g. amorphous AlCuFe[20], AlPdFe[21], $Al_{100-x}(Mn_x, Fe_x, Co_x, Ni_x)$[22]. The structure formation and stability of amorphous pure and alloy materials was deeply investi-

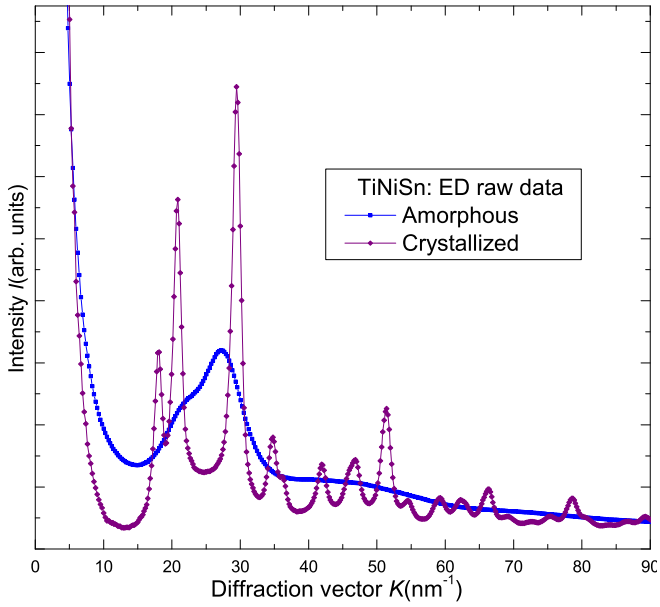

Fig. 2. Electron diffraction results of the investigated TiNiSn alloy showing the diffraction intensity raw data of the amorphous and crystallized samples.

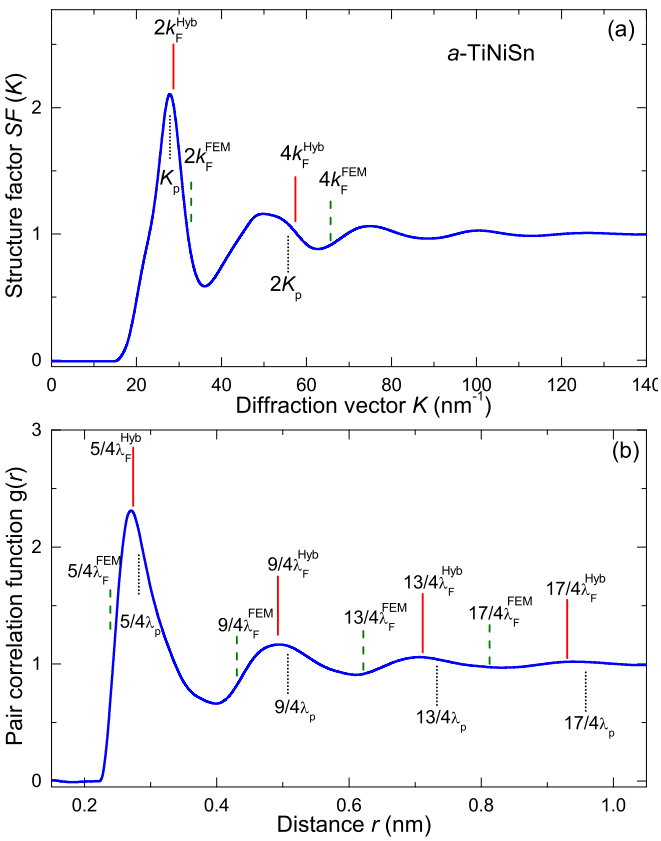

Fig. 3. Atomic structure of the amorphous TiNiSn sample. In (a) the structure factor $SF(K)$ and in (b) the pair correlation function $g(r)$ are plotted.

gated and discussed as a result of the interplay between the electrons and the ionic system forming the material in terms of Hume-Rothery phases[16]. From such analysis it was established that the above mentioned amorphous phase corresponds to elements and alloys whose atomic structures satisfy specific conditions in the K- and r-spaces. It was determined that $SF(K)$ has a dominant peak in the K-space at the diffraction vector $K_p \approx 2k_F$, with k_F the Fermi vector defined as $k_F = \sqrt[3]{3\pi^2 n_0 Z_{eff}}$, being n_0 the mean particle density and Z_{eff} the mean valence per atom in the alloy. The value n_0 can be calculated from the element's density in the liquid state or estimated from the diffraction experiment, i.e. from the reduced atomic distribution $G(r) = 4\pi r n_0[g(r) - 1]$, as shown in Fig. 4a. Z_{eff} is calculated from the valence of the corresponding elements that form the alloy.

It has also been established that in r-space the distance between the nearest-neighbors positions in the pair correlation function $g(r)$, i.e. between two adjacent peaks, satisfies that $2\pi/K_p = \lambda_p \approx \lambda_{Fr}$, being the Friedel wavelength $\lambda_{Fr} = 2\pi/2k_F$. In other words, it was determined that in the above-mentioned alloys the expressions $K_p \approx 2k_F$ and $\lambda_p \approx \lambda_{Fr}$ induce a spherical periodic order (SPO) and the positions of the nearest neighbors in $g(r)$ are well described by $r_{n+1} = (5/4 + n) \cdot \lambda_p$, ($n$ = 0,1,2,..) [16].

In order to understand the atomic structure, stability and transport properties of our amorphous TiNiSn film, we checked the SPO formation rules. First, it can be observed that the sample displays a dominant peak in $SF(K)$ at the position named K_p, and a second peak at $\approx 2K_p$ (Fig. 3a), similarly to other amorphous materials[22,23]. If we calculate the nearest-neighbors position in $g(r)$ using $r_{n+1}^{\lambda_p}$ with $\lambda_p = 2\pi/K_p$, the maxima in $g(r)$ are relatively well described, which is shown as vertical dotted lines in Fig. 3b. Therefore, from the analysis of $SF(K)$ and $g(r)$, it is possible to conclude that the amorphous TiNiSn satisfies the SPO structure formation.

Next, we are interested in finding out if $K_p \approx 2k_F$ and $\lambda_p \approx \lambda_{Fr}$ are verified in the TiNiSn alloy. From the reduced atomic distribution $G(r)$ shown in Fig. 4a we obtained the experimental value $n_0^{exp} = 52.1\,\mathrm{nm}^{-3}$ (from the slope for $r < r_1$), while considering the density of the components in the liquid state yields $n_0 = 49.88\,\mathrm{nm}^{-3}$. Similar results were observed in many other amorphous materials, pure metals and alloys [24,25]. This conclusion is important to support our assumptions, because it was reported that some amorphous materials reach the stability by a drastic change of the mean particle density in order to satisfy the SPO structure formation, e.g. in the amorphous $Na_{100-x}Sn_x$ [26] a change of 50 % in n_0^{exp} was observed, as compared to the calculated value using the material's density in the liquid state.

We now draw the attention to the atomic structure of the previously mentioned family of amorphous alloys containing one TM with d valence electrons. In the first analysis, when the structure formation with SPO was confirmed, it was established that the following conditions are satisfied: having a dominant peak in $SF(K)$ at K_p and being λ_p the distance between nearest-neighbors in $g(r)$. Now we need to establish if the relations $K_p \approx 2k_F$ and $\lambda_p \approx \lambda_{Fr}$ are satisfied. In a previous paper[22] the alloy $Al_{100-x}Fe_x$ was studied. In this case, if the Z_{eff} valence for aluminum $Z_{Al} = 3\,e/a$ and for iron $Z_{Fe} = 1\,e/a$ were used to calculate k_F, the equalities $K_p \approx 2k_F$ and $\lambda_p \approx \lambda_{Fr}$ completely failed, while if hybridization effects were considered, not only the atomic structure in inverse K- and real r-space were well described, but also the electronic transport properties and phase stability were well understood. Summarizing, it was established that when Al is alloyed with a transition metal such as Mn, Fe, Co or Ni, during the structure formation these elements should be considered with a negative valence, i.e. $Z_{Mn} = -5\,e/a$, $Z_{Fe} = -4\,e/a$, $Z_{Co} = -3\,e/a$ and $Z_{Ni} = -2\,e/a$ [22,23]. Next, in order to calculate k_F we need to estimate Z_{eff}. If we assume the valences: $Z_{Ti} = 4\,e/a$, $Z_{Ni} = 1\,e/a$ and $Z_{Sn} = 4\,e/a$ for Ti, Ni and Sn respectively, we obtain $Z_{eff} = 3\,e/a$. Using the experimental value n_0^{exp} and $Z_{eff} = 3\,e/a$ it is possible to calculate k_F^{FEM}, λ_{Fr}^{FEM} and r_{n+1}^{FEM} (where the upper-index 'FEM' stands for free electron model) and the results are plotted as vertical dashed lines in Fig. 3a and Fig. 3b. It is evident that the so-estimated values can't satisfactorily explain the

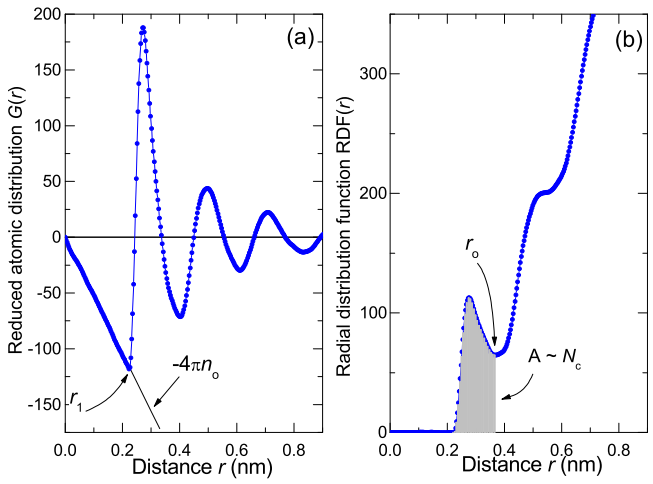

Fig. 4. (a) Reduced atomic distribution $G(r)$ and (b) radial distribution function RDF of the amorphous phase.

structure data in the K- and r-space. In search of a better agreement between calculated and experimental data, we consider the results obtained in Ref. [22] and assume $Z_{\rm Ni} = -2\,e/a$, Ti and Sn with same valence as before, so the total $Z_{\rm eff} = 2\,e/a$. Under this assumption we calculate $k_{\rm F}^{\rm Hyb}$, $\lambda_{\rm Fr}^{\rm Hyb}$ and $r_{n+1}^{\rm Hyb}$ (where the upper-index 'Hyb' means hybridization). The results of this calculation are plotted as vertical red solid lines in Fig. 3a and Fig. 3b. Under the assumption of hybridization we can describe very well the main peak in $SF(K)$ as well as the nearest neighbors positions in $g(r)$, i.e. $K_p \approx 2k_{\rm F}^{\rm Hyb}$, $\lambda_p \approx \lambda_{\rm Fr}^{\rm Hyb}$ and $r_{n+1}^{\lambda_{\rm p}} \approx r_{n+1}^{\rm Hyb}$. The question now is how to understand that Ni contributes with a negative valence to the TiNiSn alloy. To explain this we have listed in Table I the electron configuration and the electronegativity χ according to the Pauling scale of the forming elements. According to these values, in order to fill the d states, Ti needs 8 and Ni needs 2 electrons, respectively. By considering the electronegativity difference between the components, i.e. $\chi_{\rm Sn} - \chi_{\rm Ti} = 0.42$, $\chi_{\rm Sn} - \chi_{\rm Ni} = 0.05$ and $\chi_{\rm Ni} - \chi_{\rm Ti} = 0.37$, we can conclude that Ti finds it easier to lose its electrons, by hybridization with the s,p-Sn electrons or by filling the two electrons that Ni needs to get a $3d^{10}$ configuration. Considering the theoretical and experimental studies done on hybridization in amorphous and quasicrystalline alloys [27,28], we are inclined to assume that the two $3d^2$ electrons from Ti are used to fill the two missing d electrons from Ni, so the alloy has a full $3d$ band. This electronic configuration cancels the material's magnetic properties out, as recently shown in amorphous Al_xFe_{100-x} [29], and earlier in quasicrystalline AlCuFe [20] and AlPdFe [21], when a full d band is obtained by hybridization and the alloy does not show ferromagnetic properties. Similar arguments were used to explain why the HH alloys TiCoSb and TiNiSn are non-magnetic materials [30,31].

Another parameter in amorphous and liquid systems

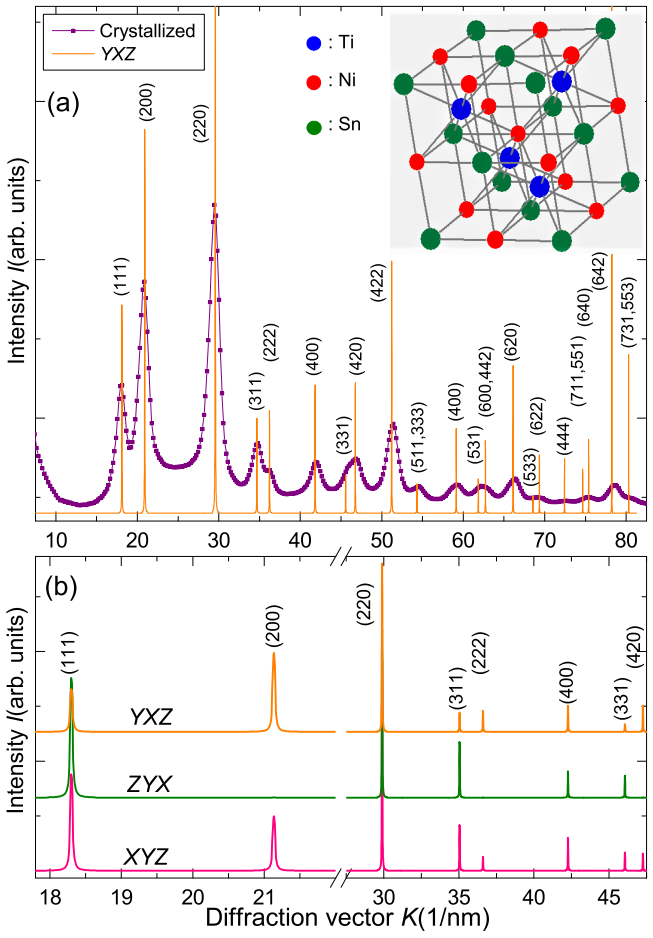

Fig. 5. (a) Atomic structure of the crystallized TiNiSn sample (ED data). The solid lines correspond to the X ray diffraction peaks simulated considering a space group $F\bar{4}3m$ for crystalline TiNiSn. Miller indexes are shown on the corresponding reflection. The inset shows the crystalline structure and elements occupation. (b) Calculated XRD patterns for the three atomic configurations.

which gives information about the local order is the coordination number N_c which, in the case of highly packed structures such as hexagonal or icosahedral local order, is between 10 to 12. From the integral of the first peak in the radial distribution function (RDF) we can calculate N_c using the following equation $N_c = \int_0^{r_o} 4\pi r^2 n_0 g(r)\,dr$, where r_o is the minimum after the first peak in the radial distribution function RDF. In Fig. 4b the RDF is plot-

TABLE I. Electron configuration and Pauling electronegativity of TiNiSn forming elements.

Element	Electron Configuration	Electronegativity χ
Titanium	[Ar] $3d^2 4s^2$	1.54
Nickel	[Ar] $3d^8 4s^2$	1.91
Tin	[Kr] $5s^2 4d^{10} 5p^2$	1.96

ted and the shaded region indicates the area that was used to determine the coordination number $N_c = 11 \pm 1$; this value indicates that the amorphous TiNiSn film has a densely packed structure, similar to other amorphous materials containing TM elements[21]. It is worth commenting that it has been found that the more densely packed the structure is in the amorphous phase than in the crystalline one, superconductivity is promoted in Bi, Ga, Sn and Be[32,33], while in their crystalline phases they are not superconductors; in the case of Pb, the behavior is the opposite [34].

In order to further characterize the prepared material, one of the samples deposited on a TEM grid (see Fig. 1) was annealed *ex-situ* up to $T = 850\,\mathrm{K}$ and ED measurements were performed on the crystallized sample. The results are plotted in Fig. 2 and in Fig. 5. It is well known that the TiNiSn alloy crystallizes in the non-centrosymmetric MgAgAs structure type with space group $F\bar{4}3m$ (No. 216). To analyze the results, the possible congurations of the constituent atoms within the unit cell can be written in the same notation used by Larson *et al.*[35]. In this notation, the Ni atom is denoted as X, the Ti atom as Y, and the Sn atom as Z. The order of X, Y, and Z tells the relative positions of the atoms within the cell. The first letter refers to the atoms with octahedral coordination located at the position $(1/4, 1/4, 1/4)$ while the second letter refers to the atom at position $(1/2, 1/2, 1/2)$, and the third one refers to the atom at position $(0, 0, 0)$. According to the theoretical calculations of Larson *et al.* [35], the configuration XYZ (a=5.959 Å) has the lowest energy, followed by ZYX (a=6.094 Å) and YXZ (a=6.135 Å). The XYZ (NiTiSn) forms a narrow-gap semiconductor, ZYX (SnTiNi) structure forms a zero-gap semiconductor and the highest-energy conguration YXZ (TiNiSn) renders a metallic system[35,36].

The peak positions measured by ED can be compared with the positions of the reflection peaks obtained by simulating an XRD pattern with the same incident wavelength, since the structure factor is the same for both techniques[37]. Using an online free software (PowderCell 2.4) we have simulated the X-ray diffraction patterns for TiNiSn assuming the three different configurations, i.e. XYZ, ZYX and YXZ. As shown by the vertical lines in Fig. 5a, which correspond to the simulated reflections of the YXZ structure, we can deduce that this is the configuration which best describes our experimental results, with a lattice parameter of $a = 6.01$ Å. Our estimated lattice parameter is close to the experimental value of a sample prepared by rapid solidification $a = 5.946$ Å (YXZ)[38].

The following reasons support the conclusion that our TiNiSn sample has the YXZ crystalline structure:

1. The XRD simulations for the three different configurations of the crystalline structure are plotted in Fig. 5b. The peaks corresponding to reflections (200), (222) and (420) have negligible intensities for configuration ZYX but are appreciable in our pattern; this allows to discard the ZYX structure for our sample. Also, configurations XYZ and ZYX display the maximum intensity at reflection (111), unlike our sample whose maximum intensity peak corresponds to reflection (220), which is expected only for configuration YXZ. All the experimental peaks for our sample match both intensities ratio and position, of configuration YXZ.

2. The second reason is based on the observation of Aversano *et al.*[38], who find that a large amount of TiNiSn in rapidly solidified samples derives from the high undercooling rate of the liquid during the rapid solidification. This inhibits the formation of other phases and as a consequence, the metastable liquid directly solidies as TiNiSn. It is worth mentioning that our TiNiSn sample is prepared by solidification from the gas phase which probably favors the TiNiSn local atomic configuration in the amorphous state, maintaining the same local order throughout crystallization.

3. Theoretical results of Ishida *et al.* [36] and Larson *et al.* [35], have predicted a metallic behavior for the structural configuration YXZ; thus, considering our diffraction results in which the local atomic structure of the amorphous and the crystalline phases show similarities, we assume that YXZ is the atomic configuration in both phases (crystalline and amorphous) and we will show in the following section that our amorphous TiNiSn sample is metallic, supporting this conclusion.

In this section we have shown that our preparation method allows to obtain TiNiSn in the amorphous phase and after annealing at high temperatures a well-ordered crystalline phase was obtained. A detailed analysis comparing our experimental results and those of the XRD simulation, lead to the conclusion that the obtained crystalline structure corresponds to the atomic configuration YXZ. The fact that the system crystallizes as YXZ instead of the most stable XYZ phase (according to the theoretical calculations) is possibly because the annealing process is not able to induce enough atomic diffusion and the material stays in the metastable phase YXZ, extending the same local order as in the amorphous state to the whole film after crystallization.

B. Electrical transport properties

1. *Resistance as function of the temperature*

In Figure 6 we present the resistance $R(T)$ of pure amorphous TiNiSn measured immediately after condensation, during and after annealing at different temperatures T_{ann} up to 345 K. After reaching each T_{ann} the sample was cooled down to 1.2 K and the $R(T)$ was measured again. The irreversible part of the $R(T)$ (indicated with $\longrightarrow$ in Fig. 6) is characterized by a slight increase of the

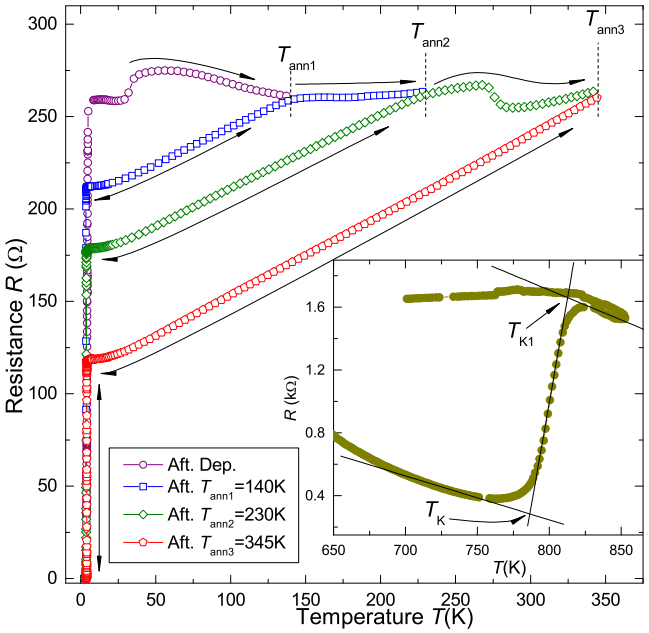

Fig. 6. Resistance of the *in-situ* prepared TiNiSn film, measured immediately after preparation and during annealing. Symbols: $\longrightarrow$ irreversible changes; $\longleftrightarrow$ reversible changes of the resistance. The inset shows the $R(T)$ at high temperatures, with the crystallization temperature of the TiNiSn amorphous sample.

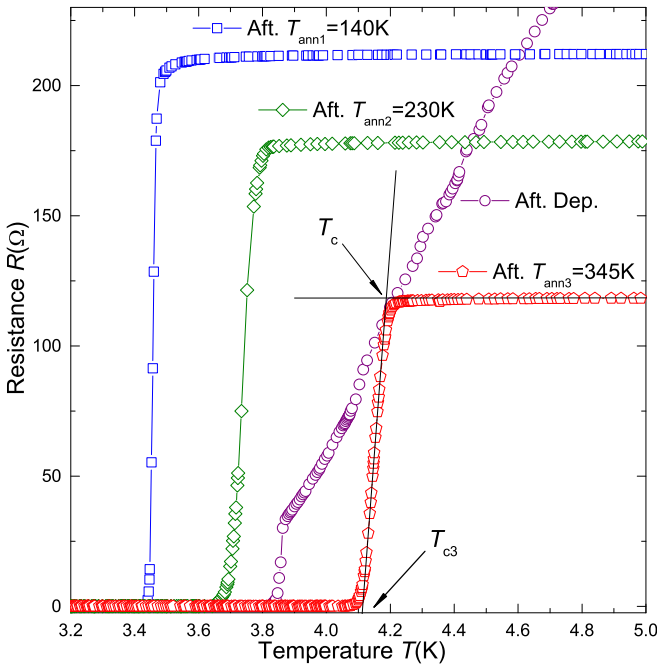

Fig. 7. Resistance measurements of the amorphous TiNiSn, showing the superconducting transition immediately after quenching and after different annealing temperatures T_{ann}.

resistance, while the reversible part ($\longleftrightarrow$ in Fig. 6) shows a systematic decrease when increasing the annealing temperature T_{ann}. A peculiar characteristic of this alloy is that after each annealing it displays a linear temperature dependence of $R(T)$, with a positive temperature coefficient $\alpha = \mathrm{d}R(T)/\mathrm{d}T$. This linear behavior corresponds to a metallic response and can be observed from temperatures $T > 20\,\mathrm{K}$ up to the corresponding T_{ann}. During cooling, the mentioned metallic behavior decreases, saturates at low temperatures and suddenly drops to zero, as shown in Fig. 7. We identify this drop in $R(T)$ as a superconducting transition. The superconducting transition temperature T_{cj} $(j = 1, 2, 3)$ is defined by the intersection of the lines fitting the resistance before and immediately after the resistance drops; the width of the transition is estimated as the difference $\Delta T_{cj} = T_{cj} - T_j$, where T_j is the point of intersection between the line fitting the transition after annealing at T_{annj} with the T-axis. The T_c and $\Delta T_{c3} = T_{c3} - T_3$ after annealing at $T_{ann3} = 345\,\mathrm{K}$ are shown in Fig. 7. The estimated T_{cj} and $\Delta T_{cj} = T_{cj} - T_j$ vs. the annealing temperature are plotted in Fig. 8a and Fig. 8b, respectively. We can readily see from Fig. 7 that immediately after preparation, the sample has a $T_{c0} = 3.86\,\mathrm{K}$, which is greater than the $T_{c1} = 3.47\,\mathrm{K}$ and $T_{c2} = 3.78\,\mathrm{K}$ obtained after the two first annealing steps, but less than after the third annealing with $T_{c3} = 4.19\,\mathrm{K}$. Because T_{c0} is irreversible immediately after deposition, we will focus on discussing the T_c's after each annealing. A nearly linear relationship in T_{cj} vs T_{ann} can be observed in Fig. 8a, indicating that the effect of annealing (besides improving the local atomic structure), helps to increase the T_c, contrarily to the usual observation of a decrease in the T_c after annealing (e. g. in amorphous Bi and $\mathrm{Bi}_{100-x}\mathrm{Sb}_x$ [39]). To the best of our knowledge, this is an unusual behavior and has not been reported by other authors.

In a next step to quantify the effect of annealing on the transport properties, we have estimated the resistivity ρ at $T = 125\,\mathrm{K}$ and the temperature coefficient of the resistance $\alpha = \mathrm{d}R(T)/\mathrm{d}T$ after each T_{ann}. The estimated $\rho(T = 125\,\mathrm{K})$ and the coefficient α are plotted in Fig. 8a and Fig. 8b, respectively. Our resistivity value is of the same order as reported in other transition-metal-based amorphous superconductors such as $\mathrm{Zr}_x(\mathrm{Fe,Ni,Co})_{100-x}$ alloys [40,41].

Analyzing the resistivity results, we can affirm that after each annealing the sample's resistivity decreases and the coefficient α increases. This can be understood taking into account the Faber-Ziman [42] theory, which considers that during the annealing process the atoms move to more favorable positions increasing the local- and medium-range order, with the consequence of increasing the amount of electrons at the Fermi level in the density of states; this decreases the resistivity and increases the electron-phonon interaction, therefore leading to an increase of the coefficient α. This elucidation supports our findings at temperatures $T < 20\,\mathrm{K}$, i.e. the increase of the superconductivity temperature transition T_c after each annealing. The crystallization

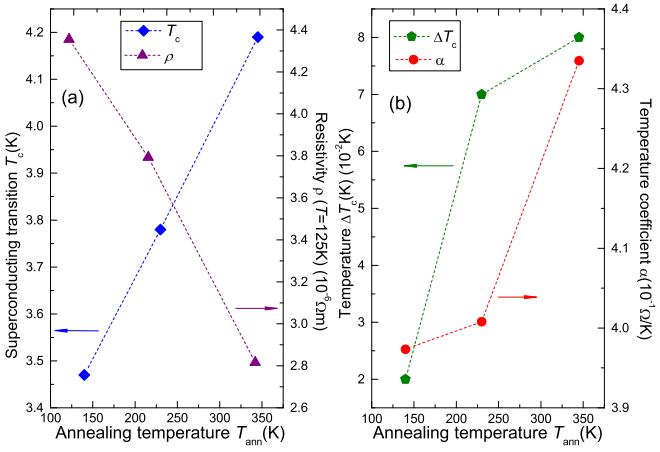

Fig. 8. Resistivity and superconducting parameters. In (a) the transition temperature T_c and the resistivity $\rho(T = 125)$ K are plotted. The width of the transition temperature ΔT_c and the temperature coefficient α are displayed in (b).

temperature T_K of the amorphous phase was determined through resistance measurements. For that purpose, a deposited sample with a four-point electrode configuration (as sketched in Fig. 1a) was annealed *ex-situ* in a high-temperature chamber with a nominal pressure of $P \approx 10^{-7}$ mbar, up to $T = 850$ K and the resistance was measured as the heat treatment proceeded. The results are presented in the inset of Fig. 6, from the curve $R(T)$ we can estimate the crystallization temperature as the point where a sharp change in ~~the~~ $R(T)$ occurs at $T_{\rm K} \approx 785$ K and the estimated crystallization temperature width $\Delta T_{\rm K} = T_{\rm K1} - T_{\rm K} = 27$ K (see inset of Fig. 6). The $\Delta T_{\rm K}$ observed in our TiNiSn sample is similar to that of amorphous alloys with local icosahedra order, which after annealing transform into the ordered quasicrystalline structure as observed in AlCuFe[20], AlPdRe[43] and AlPdFe[21]. The $T_{\rm K}$ of the amorphous TiNiSn is higher than the crystallization temperature of amorphous Sn_{1-x}(Au, Ag, Cu)$_x$[16], but comparable to those alloys which are structurally stabilized by hybridization, such as Al_{1-x}(Mn, Fe, Co, Ni)$_x$[22] alloys and ternary quasicrystals such as AlCuFe[20], AlPdRe[43] and AlPdMn[44].

2. *Thermopower as function of the temperature*

The thermopower $S(T)$ temperature dependence of the investigated TiNiSn sample is shown in Fig. 9a. the S(T)

after quenching, during and after annealing is negative; at temperatures $T > 100$ K the $S(T)$ is almost linear and decreases slightly in magnitude with increasing annealing temperature. Our $S(T)$ results at temperatures $T < 75$ K are remarkable since a deep hump is observed, with a minimum at $T \approx 18.5$ K, almost constant for the different annealings. In many non-magnetic amorphous materials, pure and alloys, the reported thermopower is linear with temperature[24,45] and near to the value predicted by the Mott equation. This equation considers that the scattering of the electrons is elastic and the density of states is reasonably smooth, so the diffusion thermopower $S(T)_D$ is a linear function of temperature, starting at the origin with a negative sign[46], which is not case for our investigated material. From the early days of thermopower research, the temperature dependence of amorphous metals thermopower $S(T)$ was considered particularly interesting since phonon-drag should be negligible in these materials. The explanation was that the scattering of phonons by conduction electrons is much weaker than in crystals due to the high degree of disorder, so that phonons are essentially in thermal equilibrium.

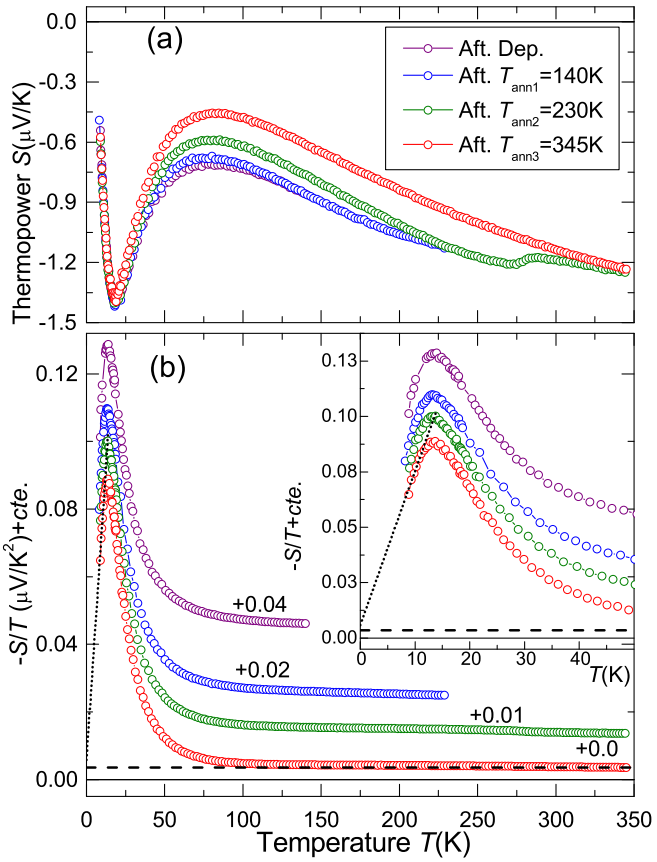

Fig. 9. Thermopower $S(T)$ (a) and $-S(T)/T$ (b) after different annealings. In (b), the curves are shifted vertically for clarity. The inset is a zoom of the low temperature region. The dotted and dashed lines in the inset and in the main figure correspond to the extrapolations $(-S(T)/T)_{T\to 0}$ (dotted lines) and $(-S(T)/T)_{T\to\infty}$ (dashed lines), respectively.

According to the literature, the hump in $S(T) < 75$ K can be originated by impurities (Kondo effect[47]) or by the phonon-drag effect[48]. A hump in the thermopower of non-magnetic materials because of the presence of magnetic impurities such as Fe, Co, Ni (in ppm range) was observed and explained on the basis of the Kondo effect in crystalline (e. g. Au [49,50], Cu [47]) and amorphous

(e.g. PdSi[51]) materials. This behavior is accompanied by a minimum in the resistivity at the same temperature range as the hump in $S(T)$, and usually at very low temperatures ($T < 5\,\mathrm{K}$). On the other hand, in amorphous magnetic alloys such as $Be_{40}Ti_{50}Zr_{10}$ [52] and $Fe_{80}B_{20}$ [53], the thermopower is found to be far from linear, but it behaves smoothly and shows changes in the slope at temperatures $T > 200\,\mathrm{K}$.

The existence of phonon-electron interactions in amorphous materials is currently well accepted and it is used to explain phonon-mediated superconductivity in amorphous and even the increase of T_c in crystalline superconductors due to the disorder [54]. It is worth mentioning that short wavelength collective excitations from transverse acoustic waves in amorphous $Mg_{70}Zn_{30}$ [55] were measured and explained as arising from diffusing Umklapp scattering process [56], a mechanism that was only believed to exist in crystalline solids. In order to explain the thermopower enhancement observed in our results we can refer to previous studies on many amorphous [57,58] and crystalline high temperature superconductor materials [59–62], in which the increase of $S(T)$ at low temperatures, before the sample enters in the superconducting state, is due to electron-phonon enhancement effects. In the specific case of amorphous materials, it was suggested that the electron-phonon interaction enhances the low temperature $S(T)$ by the factor $(1 + \lambda_{e-p}(T))$, where λ_{e-p} is the electron-phonon mass enhancement [57,58,63,64]. Considering that the thermopower is enhanced because of the electron-phonon mass enhancement, we have:

$$\frac{S(T)}{T} = \frac{S_D(T)}{T}\Big[1 + \lambda_{e-p}(T)\Big], \qquad (1)$$

and the ratio

$$\left(\frac{S(T)}{T}\right)_{T\to 0} \Big/ \left(\frac{S(T)}{T}\right)_{T\to\infty} = \Big[1 + \lambda_{e-p}(0)\Big], \qquad (2)$$

with $\lambda_{e-p}(0)$ a constant which can be estimated from thermopower results. For this purpose we have plotted $S(T)/T$ vs T in Fig. 9b and we have estimated $(S(T)/T)_{T\to 0}$ and $(S(t)/T)_{T\to\infty}$; the dashed lines in Fig.9b and its inset indicate how the extrapolations were made. Because the limits of $(S(T)/T)_{T\to 0,\infty}$ can be more accurately estimated for the sample annealed up to $T = 345\,\mathrm{K}$, we estimate $\lambda_{e-p}(0)$ for this annealing and use it later for comparison. We get $(S(T)/T)_{T\to 0} = 0.0057$ and $(S(T)/T)_{T\to\infty} = 0.0035$, which give $\lambda_{e-p}(0) = 0.62$, a value which indicates an intermediate electron-phonon coupled superconductor. The best available theory of superconductivity in metals is the well-known BCS-Eliashberg-McMillans formalism for metallic superconductors[65]. The use of MacMillan equation to obtain a good estimate of the superconducting parameters of different alloys is supported by many experimental [34,66,67] as well as theoretical [34,39,68] works in the literature. According to this theory, the superconducting transition can be expressed as:

Alloy	T_c(K)	$\lambda_{e-p}(0)$	Reference
Amorphous			
a-TiNiSn	4.19	0.6	This work
a-$Cu_{1-x}Zr_x$	$0.31 - 3.18$	$0.507 - 0.818$	Ref. [40]
a-$Ni_{1-x}Zr_x$	$0.3 - 3.97$	$0.825 - 0.976$	Ref. [40,70]
a-$Fe_{1-x}Zr_x$	$0.6 - 3.3$	$0.913 - 0.981$	Ref. [40,41]
a-$Co_{1-x}Zr_x$	$0.70 - 4.001$	$0.948 - 1.015$	Ref. [41]
a-$Fe_xNi_{1-x}Zr_2$	$0.2 - 2.6$	≈ 0.6	Ref. [69]
Crystalline - HH alloys			
LaPtBi	0.76	0.4	Ref. [71]
YPtBi	0.77	0.46*	Ref. [72]
LuPdBi	1.7	0.54*	Ref. [73]
TbPdBi	1.7	0.54*	Ref. [74]
HoPdBi	0.7	0.46*	Ref. [75]
ScPtBi	0.7	0.45*	Ref. [76]
LuPtBi	1.0	0.46*	Ref. [9]
Crystalline - FH alloys			
YPd_2Sn	4.7	0.7	Ref. [6]
$MgPd_2Sb$	2.2	0.53	Ref. [77]
$ZrNi_2Ga$	2.9	0.55	Ref. [78]
$NbNi_2$(Al,Sn)	2.15, 2.9	0.51, 0.61	Ref. [79]

TABLE II. The superconducting transition temperature T_c and the estimated $\lambda_{e-p}(0)$ of some amorphous, and crystalline HH and FH alloys. The values of $\lambda_{e-p}(0)^*$ marked with an asterisk were not reported in the corresponding reference and were obtained using McMillan's equation (Eq. 3), the reported values of T_c, the Debye temperature (calculated as we did for our TiNiSn sample) and we assumed $\mu^* = 0.13$.

$$T_c = \frac{< w >}{1.2} \exp\left[\frac{-1.04(1 + \lambda_{e-p})}{\lambda_{e-p} - \mu^*(1 + 0.62\lambda_{e-p})}\right] \qquad (3)$$

where $< w >$ is the average phonon frequency and μ^* is an electron-electron Coulombic interaction parameter. We use McMillan's approximation[65] that $< w >= 0.828\,\theta_D$, with θ_D the Debye temperature. More problematic is the choice of μ^*, which for transition metals normally lies between 0.1 and 0.17 [65]. Having the T_c from resistance measurements, we can apply Eq. 3 to calculate $\lambda_{e-p}(0)$; for that purpose we have estimated the Debye temperature from the θ_D of the individual elements of the alloy using the Kopp-Neumann relation, so we get $\theta_D = 272\,\mathrm{K}$. For the electron-electron Coulombic interaction parameter we used the value of $\mu^* = 0.13$ [40,69]. Then, we obtain $\lambda_{e-p}(0) = 0.59$ for the T_c after the third annealing (T_{c3}). Finally, we can affirm that the electron-phonon $\lambda_{e-p}(0)$ estimated from the thermopower and resistance measurements are of the same order of magnitude, which leads us to state that the superconductivity in the amorphous phase of TiNiSn is a consequence of the electron-phonon mass enhancement and the magnitude indicates that the amorphous TiNiSn is an intermediate electron-phonon coupled superconductor.

Our estimated $\lambda_{e-p}(0)$ of the amorphous TiNiSn is very similar to that from other amorphous, as well as

other HH and FH alloys; representative values are listed in Table II. As it is evident, the T_c of amorphous TiNiSn is the highest amongst the crystalline HH alloys and in the same order of the FH alloys (only overcome by YPd_2Sn [6]); $\lambda_{e-p}(0)$ is in the same order as the obtained for FH and HH alloys. This result lead us to conjecture that crystallized TiNiSn from the amorphous and low annealing after crystallization (to obtain the atomic position YXZ in the elemental cell as we have obtained) should be superconducting and probably with a higher T_c than in the amorphous state. Verification of this hypothesis is a task which remains to be investigated in the future, as well as the study of another amorphous HH alloys.

IV. CONCLUSION

Using the simple and versatile technique of flash evaporation we have prepared an amorphous thin film of the HH alloy TiNiSn. Resistance measurements show that TiNiSn in the amorphous phase exhibits a linear metallic behavior and is a superconductor, and that increasing the annealing temperature increases the T_c instead of destroying it. The thermopower at $T < 75\,\mathrm{K}$ is very well understood in terms of electron-phonon mass enhancement. The estimated $\lambda_{p-e}(0)$ using both $S(T)$ and T_c values from $R(T)$ data are similar and suggest that amorphous TiNiSn is an intermediate electron-phonon coupled superconductor. Well-ordered spherical periodic order and high stability of the amorphous phase support our interpretation that hybridization plays an important role in the properties of amorphous TiNiSn. After annealing up to $T = 850\,\mathrm{K}$ the sample crystallizes and shows a well-ordered crystal structure with space group $F\bar{4}3m$ and atomic positions in the unit cell TiNiSn (YXZ), differently as usually found (XYZ), when other methods of preparation are used. We believe that our preparation method can help to explore the properties of this and other HH alloys with non-centrosymmetric crystallographic symmetry, in which different atomic positions can be reached and new physical properties could be explored.

ACKNOWLEDGMENTS

P. G. B. acknowledges partial funding from ANPCyT-Foncyt and Secyt-UNC (Argentina). L. V. acknowledges a post-doctoral fellowship from Conicet, Argentina.

* j.barzola@gmx.de

[1] F. Heusler, Verhandlungen der Deutschen Physikalischen Gesellschaft **5**, 219 (1903).
[2] C. Felser, G. H. Fecher, and B. Balke, Angew. Chem. Int. Ed. **46**, 668 (2007).
[3] S. Sakurada and N. Shutohe, Appl. Phys. Lett. **86**, 082105 (2005).
[4] S. Chadov, X. Qi, J. Kübler, G. H. Fecher, C. Felser, and S. C. Zhang, Nat. Mat. **9**, 541 (2010).
[5] M. Ishikawa, J. L. Jorda, and A. Junod, *Superconductivity in d- and f- band metals*, edited by W. Buckel and W. Weber (Proceedings of the IV Conference, Karlsruhe, 1982).
[6] T. Klimczuk, C. H. Wang, K. Gofryk, F. Ronning, J. Winterlik, G. H. Fecher, J.-C. Griveau, E. Colineau, C. Felser, J. D. Thompson, D. J. Safarik, and R. J. Cava, Phys. Rev. B **85**, 174505 (2012).
[7] N. P. Butch, P. Syers, K. Kirshenbaum, A. P. Hope, and J. Paglione, Phys. Rev. B **84**, 220504(R) (2011).
[8] Y. Pan, A. M. Nikitin, T. V. Bay, Y. K. Huang, C. Paulsen, B. H. Yan, and A. de Visser, Europhys. Lett. **104**, 27001 (2013).
[9] F. F. Tafti, T. Fujii, A. Juneau-Fecteau, S. R. de Cotret, N. Doiron-Leyraud, A. Asamitsu, and L. Taillefer, Phys. Rev. B **87**, 184504 (2013).
[10] M.Smidman, M.B.Salamon, H.Q.Yuan, and D.F.Agterberg, Rep. Prog. Phys. **80**, 036501 (2017).
[11] J. Barzola-Quiquia, M. Stiller, P. D. Esquinazi, J. Quispe-Marcatoma, and P. Häussler, J. Magn. Magn. Mater. **456**, 281 (2018).
[12] Y. V. Kudryavtsev, V. A. O. Y. P. L. Y. H. Hyun, J. B. Kim, J. S. Park, S. Y. Park, and J. Dubowik, Phys. Rev. B **76**, 024430 (2007).
[13] Z. Zhu, T. Higo, S. Nakatsuji, and Y. Otani, AIP Advances **10**, 085020 (2020).
[14] P. Häussler, Topics Appl. Phys. **72**, 163 (1994).
[15] R. W. Cahn, *Physical Metallurgy, third edition* (Elsevier Science Publishers B.V., 1983).
[16] P. Häussler, Phys. Rep. **222**, 65 (1992).
[17] C. Lauinger, T. Hunger, J. Barzola-Quiquia, P. Häussler, and H.-G. Boyen, J. Non-Cryst. Solids **250-252**, 791 (1999).
[18] E. Compans, Rev. Sci. Instrum. **60**, 2715 (1989).
[19] H. Leitz, Z. Phys. B **40**, 65 (1980).
[20] C. Roth, G. Schwalbe, R. Knöfler, Zavaliche, O. Madel, R. Haberkern, and P. Häussler, J. Non-Cryst. Solid **252-252**, 869 (1999).
[21] J. Barzola-Quiquia, M. Stiller, M. Stiehler, P. Esquinazi, and P. Häussler, Mater. Res. Express **2**, 096403 (2015).
[22] J. Barzola-Quiquia, M. Lang, D. Decker, and P. Häussler, J. Non-Cryst. Solid **334–335**, 352 (2004).
[23] M. Stiehler, U. Giegengack, J. Barzola-Quiquia, J. Rauchhaupt, S. Schulze, and P. Häussler, J. Phys. Chem. Solids **68**, 1244 (2007).
[24] P. Häussler, Phys. Rep. **222**, 65 (1992).
[25] J. Barzola-Quiquia and P. Häussler, J. Non-Cryst. Solids **299-302**, 269 (2002).
[26] O. Madel, C. Lauinger, and P. Haussler, J. Non-Cryst. Solid **250-252**, 267 (1992).
[27] S. J. Poon, Adv. Phys. **41**, 303 (1992).
[28] E. S. Zijlstra, S. K. Bose, M. Klanjsek, P. Jeglic, and J. Dolinsek, Phys. Rev. B **72**, 174206 (2005).
[29] J. Barzola-Quiquia, E. Osmic, and P. Häussler, J. Magn. Magn. Mater. **526**, 167624 (2021).

[30] J. Pierre, R. V. Skolozdra, J. Tobola, S. Kaprzyk, C. Hordequin, M. A. Kouacou, I. Karla, R. Currat, and E. Lelievre-Berna, J. Alloy Compd. **262–263**, 101 (1997).
[31] D. Jung, H.-J. Koo, and M.-H. Whangbo, J. Mol. Struct. Theochem. **527**, 113 (2000).
[32] W. Buckel and R. Hilsch, Z. Phys. **138**, 109 (1954).
[33] A. E. Curzon and A. J. Mascall, J. Phys. C: Solid State Phys. **2**, 382 (1969).
[34] G. Bergmann, Phys. Rep. **27**, 159 (1976).
[35] P. Larson, S. D. Mahanti, and M. G. Kanatzidis, Phys. Rev. B **62**, 12754 (2000).
[36] S. Ishida, T. Masaki, S. Fujii, and S. Asano, Physica B **237–238**, 363 (1997).
[37] L. Reimer, *Scanning Electron Microscopy: Physics of Image Formation and Microanalysis* (IOP Publishing, 2000).
[38] F. Aversano, A. Ferrario, S. Boldrini, C. Fanciulli, M. Baricco, and A. Castellero, J. of Materi. Eng. and Perform. **27**, 6306 (2018).
[39] J. Barzola-Quiquia, C. Lauinger, M. Zoraghi, M. Stiller, S. Sharma, , and P. Häussler, Supercond. Sci. Technol. **30**, 015013 (2017).
[40] Z. Altounian and J. O. Strom-Olsen, Phys. Rev. B **27**, 4149 (1983).
[41] E. Batalla, Z. Altounian, and J. O. Strom-Olsen, Phys. Rev. B **31**, 577 (1985).
[42] P. Häussler, H. Nowak, M. Bhuiyan, and J. Barzola-Quiquia, Physica B **316-317**, 489 (2002).
[43] R. Haberkern, J. Barzola-Quiquia, C. Madel, and P. Häussler, MRS Proceedings **643**, K8.3 (2000).
[44] J. Barzola-Quiquia and P. Häussler, J. Non-Cryst. Solids **353**, 3237 (2007).
[45] S. R. Nagel, Phys. Rev. Lett. **41**, 990 (1978).
[46] N. F. Mott and H. Jones, *The Theory of the Properties of Metals and Alloys* (1st ed. Clarendon, Oxford, 1936).
[47] D. K. C. MacDonald and W. B. Pearson, Proc. R. Soc. Lond. A **219**, 373 (1953).
[48] D. K. C. MacDonald, W. B. Pearson, and I. M. Templeton, Proc. R. Soc. Lond. A **248**, 107 (1958).
[49] J. Kopp, J. Phys. F: Metal Phys. **5**, 1211 (1975).
[50] D. K. C. MacDonald, W. B. Pearson, and I. M. Templeton, Proc. R. Soc. Lond. A **266**, 161 (1962).
[51] P. Svoboda and P. Vasek, J. Phys. F: Metal Phys. **15**, 2489 (1985).
[52] M. N. Baibich, W. B. Muir, G. Belanger, J. Destry, H. S. Elzinga, and P. A. Schroeders, Phys. Lett. **73A**, 328 (1979).
[53] S. Basak, S. R. Nagel, and B. C. Giessen, Phys. Rev. B **21**, 4049 (1980).
[54] M. Baggioli, C. Setty, and A. Zaccone, Phys. Rev. B **101**, 214502 (2020).
[55] J.-B. Suck, H. Rudin, H.-J. Guntherodt, and H. Beck, J. Phys. C: Solid St. Phys. **13**, L1045 (1980).
[56] J. Hafner, J. Phys. C: Solid St. Phys. **14**, L287 (1981).
[57] J. Jäckle, J. Phys. F: Metal Phys. **10**, L43 (1980).
[58] J. L. Opsal, B. J. Thaler, and J. Bass, Phys. Rev. Lett. **36**, 1211 (1976).
[59] A. B. Kaiser, Phys. Rev. B **37**, 5924 (1988).
[60] A. B. Kaiser and G. Mountjoy, Phys. Rev. B **43**, 6266 (1991).
[61] L. Cohn and S. A. Wolf, Phys. Rev. Lett. **66**, 1098 (1991).
[62] A. Mawdsley, H. J. Trodahl, J. Tallon, J. Sarfati, and A. B. Kaiser, Nature **328**, 233 (1987).
[63] B. L. Gallagher and D. Greig, J. Phys. F: Met. Phys. **11**, L207 (1982).
[64] B. L. Gallagher, J. Phys. F: Met. Phys. **12**, 1721 (1981).
[65] W. L. McMillan, Phys. Rev. **167**, 331 (1968).
[66] B. L. Gallagher and B. J. Hickey, J. Phys. F: Met. Phys. **15**, 911 (1985).
[67] A. B. Kaiser, A. L. Christie, and B. L. Gallagher, Aust. J. Phys. **39**, 909 (1986).
[68] A. M. Vora, Cent. Eur. J. Phys. **6**, 263 (2008).
[69] J. Lefebvre, M. Hilke, and Z. Altounian, Phys. Rev. B **79**, 184525 (2009).
[70] F. Mahini, F. S. Razavi, and Z. Altounian, Phys. Rev. B **39**, 4677 (1989).
[71] D. Shrivastava and S. P. Sanyal, Solid State Commun. **273**, 1 (2018).
[72] T. Bay, M. Jackson, C. Paulsen, C. Baines, A. Amato, T. Orvis, M. Aronson, Y. Huang, and A. de Visser, Solid State Commun. **183**, 13 (2014).
[73] G. Xu, W. Wang, X. Zhang, Y. Du, E. Liu, S. Wang, G. Wu, Z. Liu, and X. X. Zhang, Sci. Rep. **4**, 5709 (2014).
[74] H. Xiao, T. Hu, W. Liu, Y. L. Zhu, P. G. Li, G. Mu, J. Su, K. Li, and Z. Q. Mao, Phys. Rev. B **97**, 224511 (2018).
[75] O. Pavlosiuk, D. Kaczorowski, X. Fabreges, A. Gukasov, and P. Wisniewski, Sci. Rep. **6**, 18797 (2016).
[76] O. Pavlosiuk, A. Jezierski, D. Kaczorowski, and P. Wisniewski, Phys. Rev. B **103**, 205127 (2021).
[77] M. J. Winiarski, G. Kuderowicz, K. Gornicka, L. S. Litzbarski, K. Stolecka, B. Wiendlocha, R. J. Cava, and T. Klimczuk, Phys. Rev. B **103**, 214501 (2021).
[78] J. Winterlik, G. H. Fecher, C. Felser, M. Jourdan, K. Grube, F. Hardy, H. von Lohneysen, K. L. Holman, and R. J. Cava, Phys. Rev. B **78**, 184506 (2008).
[79] S. Waki, Y. Yamaguchi, and K. Mitsugi, J. Phys. Soc. Jpn. **54**, 1673 (1985).